



Conductivity and permeability of graphite foams: Analytical modelling and pore-scale simulation

Tian Xiao^a, Xiaohu Yang^{b,*}, Kamel Hooman^c, Liwen Jin^b, Chun Yang^d, Tian Jian Lu^{e,f,**}

^a State Key Laboratory for Strength and Vibration of Mechanical Structures, School of Aerospace, Xi'an Jiaotong University, Xi'an, 710049, PR China

^b Institute of the Building Environment & Sustainability Technology, School of Human Settlements and Civil Engineering, Xi'an Jiaotong University, Xi'an, 710049, PR China

^c School of Mechanical and Mining Engineering, The University of Queensland, Brisbane, Australia

^d School of Mechanical and Aerospace Engineering, Nanyang Technological University, 50 Nanyang Avenue, 639798, Singapore, Singapore

^e State Key Laboratory of Mechanics and Control of Mechanical Structures, Nanjing University of Aeronautics and Astronautics, Nanjing, 210016, PR China

^f MITT Key Laboratory of Multifunctional Lightweight Materials and Structures (MLMS), Nanjing University of Aeronautics and Astronautics, Nanjing, 210016, PR China

ARTICLE INFO

Keywords:

Permeability
Graphite foam
Fractal analysis
Effective thermal conductivity
Pore-scale numerical simulation

ABSTRACT

Graphite foams with excellent effective thermal conductivity and large surface area have primarily constituted a new area for the emerging fields of energy conversion, conservation, and management, potentially crucial for reaching the goals of carbon neutrality and emission peak. For such energy applications, graphite foam's thermal conductivity and permeability pave the physical foundation for understanding, designing, and operating thermofluidic flows inside the porous medium. However, previous prediction models of conductivity and permeability seldomly considered the effects of random distributions of pore shape and size intrinsically induced during processing of the graphite foam. To rectify this problem, analytical models of permeability and effective thermal conductivity for graphite foam are derived based on fractal theory, being duly accounted for random distributions of pore shape and size. In parallel, pore-scale numerical simulations are carried out, providing cross-validation and shedding light on transport mechanisms at pore level. Analytical model predictions and numerical simulation results are compared with existing experimental data. Results revealed that fractal analytical models accurately predicted the permeability and conductivity of graphite foams in a porosity range from 0.686 to 0.918, with different parent ligament materials and filling fluids (e.g., air and paraffin wax).

1. Introduction

Porous media with large specific surface areas and high conducting solid skeletons have received increasing attention, particularly in energy applications. For instance, upon depositing catalyst particles on solid skeleton, the porous structure supported catalyst can take advantage of the superiorities of fluid mixing and high heat conduction of the solid skeleton [1]. A significant number of energy applications with porous reactors have been established, including fuel cells [2,3], heat storage [4–6], thermal absorption [7,8], hydrogen storage [9,10], electrochemical flow cell [11,12], and building energy management [13,14]. Common in such applications, thermofluid flow through porous skeleton with chemical reactions is a fundamental process [15,16]. Therefore, the determination, design, and operation of porous thermal reactors are

highly dependent upon permeable flow and surface heat conduction inside the porous structure.

On another front, the continuous development of power electronics industry leads to increasing demand in thermal management and hence requirement for improved heat dissipation efficiency. Aluminum and copper with high thermal conductivity are widely used as the primary material for heat exchanger constructions [17]. Often, for industrial fields like aerospace and transportation, the weight of heat exchanger becomes a critical issue. As a result, highly porous cellular aluminium and copper foams with ultralightweight attributes, high specific surface area, and relatively high effective thermal conductivity have become attractive for active cooling applications in the last two decades.

More recently, in addition to aluminium and copper foams having open cells [18,19], cellular graphite foams have also been exploited for energy and thermal management applications. These graphite foams

* Corresponding author.

** Corresponding author. State Key Laboratory of Mechanics and Control of Mechanical Structures, Nanjing University of Aeronautics and Astronautics, Nanjing, 210016, PR China.

E-mail addresses: xiaohuyang@xjtu.edu.cn (X. Yang), tjlu@nuaa.edu.au (T.J. Lu).


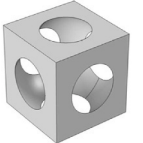

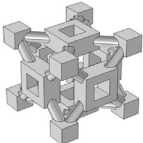
<https://doi.org/10.1016/j.ijthermalsci.2022.107706>

Received 29 January 2022; Received in revised form 15 May 2022; Accepted 18 May 2022

1290-0729/© 2022 Elsevier Masson SAS. All rights reserved.

Nomenclature			
Symbols		t	Half width of ligament (m)
a	Weight value	V	Volume (m ³)
A	Cross-sectional area of each cell (m ²)	V_{total}	Total volume (m ³)
A_p	Cross-sectional area of each pore (m ²)	V_{pore}	Pore volume (m ³)
d	Pore size (m)	V_{t-p}	Total volume of the RS (m ³)
d_E	Euclidean dimension	V_{s-p}	Total volume of ligaments within the RS (m ³)
d_s	Ligament thickness (m)	Greek symbols	
D_f	Fractal dimension of pore size distribution	λ	Pore diameter (m)
D_T	Fractal dimension of average tortuosity	ϵ	Porosity
k	Thermal conductivity (W/(m·K))	τ	Tortuosity
K	Permeability (m ²)	γ	Dimensionless parameter $\gamma = d_s/d$
L	Measurement scale (m)	Subscript	
L_0	Characteristic length (m)	av	Average
N	Number of pores	e	Effective
P	Pressure (Pa)	f	Fluid
R	Thermal resistance (K/W)	max	Maximum
R_{chain}	Thermal resistance of a chain (K/W)	min	Minimum
RD	Relative deviation	RS	Representative structure
S	Surface area (m ²)		

Table 1
Unit cell models of effective thermal conductivity for graphite foams.

Reference	Unit cell	Expression	Comments
Druma et al. [34]		$k_{eff} = k_s(1 - P/100)^{1/n}$ where $P = 100 \frac{V_{void}}{V_{total}}$	<ul style="list-style-type: none"> - Semi-analytical solution - When porosity (ϵ) is very low, $n = 2/3$; when $0.60 < \epsilon < 0.95$, $n = 0.77$ - Not suitable for the full porosity range - Periodic distribution assumed
Yu et al. [35]		$k_e = (1 - 2t + 2t^2) \frac{(1/t - 1)^2 + \sigma k_f + 2t(1-t)k_s}{(1/t - 1)^2 + 1 + (1-t)\sigma + t}$ where $\epsilon = 1 - 3t^2 + 2t^3$	<ul style="list-style-type: none"> - Analytical solution based on simplified equivalent solid square bar structure - Valid range of porosity: $\epsilon = 0.72 - 0.88$ - Periodical distribution assumed
Leong and Li [36]		$k_e = k_{eu}\gamma_{at} + k_{em}(1 - 2\gamma_{at}) + k_{eb}\gamma_{at}$ where $\gamma_{at} = t/a$	<ul style="list-style-type: none"> - Analytical solution based on thermal and electrical resistances - Valid range of porosity: $\epsilon = 0.77 - 0.88$ - Periodic distribution assumed
Chai et al. [37]		$k_e = \frac{L_A + L_B + L_C + L_D + L_E + L_F}{\frac{L_A}{k_A} + \frac{L_B}{k_B} + \frac{L_C}{k_C} + \frac{L_D}{k_D} + \frac{L_E}{k_E} + \frac{L_F}{k_F}}$	<ul style="list-style-type: none"> - Analytical solution based on thermal resistance model - Not suitable for the full porosity range - Periodic distribution assumed
Klett et al. [24]	N/A	$k_e = \alpha \left(\frac{\rho_{bulk}}{\rho_s} \right)^m k_s$ where $\alpha = 0.734$, $m = 1.427$	<ul style="list-style-type: none"> - Empirical correlation - Valid range of porosity: $\epsilon = 0.72 - 0.88$

have relatively low density (0.2–0.6 g/cm³) [20], high porosity (75–90%) [21], high specific surface area (5000–50000 m²/m³) [21] and, in particular, excellent effective thermal conductivity (40–160 W/(m·K)) as the thermal conductivity of graphite materials range from 800 to 1900 W/(m·K) [22]. In comparison, the effective thermal conductivity of aluminium foam is only 2 to 26 W/(m·K), for the thermal conductivity of aluminium varies from 140 to 237 W/(m·K) [23]. Further, when weight is of critical concern, the thermal conductivity to weight ratio is greater than 200 for graphite [24], much larger than that (45) of copper or that (54) of aluminium [17]. Therefore, highly porous

graphite foams with attributes of ultralightweight, high specific surface area, and high effective thermal conductivity have become attractive for thermal management [22], active cooling of power electronics [25,26], electromagnetic shielding [27,28], thermal energy storage [29–31], and etc. The key process in the above energy applications is fluid flow and interstitial heat transfer inside pore space. Understanding the physical mechanisms of fluid flow and interstitial heat transfer inside the pore space is essential for practical applications. In addition, at the macroscopic scale, it is of significance to determine its permeability and effective thermal conductivity as well as quantify the effects of

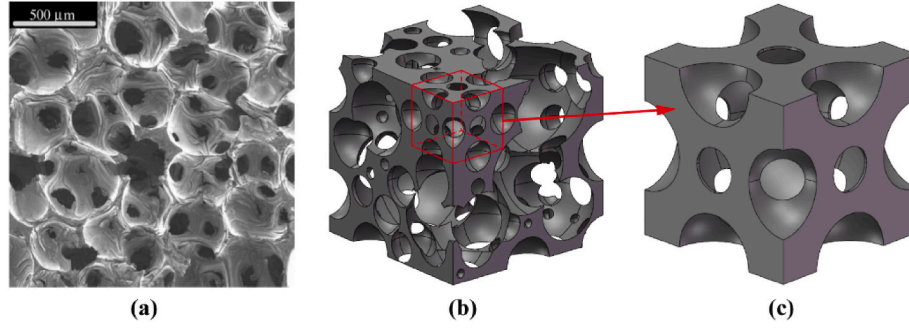


Fig. 1. Graphite foam: (a) scanning electron microscope (SEM) image of graphite foam [24]; (b) idealized cubic with random pore size and distribution; (c) representative structure (RS).

fundamental morphological parameters, since they characterize how fluid and heat are transported in the graphite foam.

To model the microstructure of a graphite foam consisting of randomly distributed ligaments that form interconnected pores, either analytically or numerically, previous efforts have been largely mainly made to construct a representative periodic unit cell (UC) with an idealized topology. Once a UC is selected for a specific foam, there are currently two common methods to calculate its permeability and effective thermal conductivity.

- 1) One is to modify the generalized models originating from packed beds to fit the experimental results of other porous media with distinctive pore structures. The Kozeny-Carmen equation [32] and the Maxwell-Eucken equation [33] are two models that are commonly applied to calculate permeability as well as effective thermal conductivity for a wide range of porous media. Although these extensions of classical models for packed beds could obtain satisfactory predictions for other types of porous media, empirical or fitting parameters are present in the Kozeny-Carmen model of permeability and the Maxwell-Eucken model of conductivity. Such parameters often vary from one type of porous medium to another and have no physical meanings.
- 2) The other method to determine the UC of a porous medium is based on the morphological and topological reconstruction of its pore-scale structure. Specifically, for graphite foams, Table 1 summarizes the various UC-based prediction models of effective thermal conductivity developed. At present, the models for the effective thermal conductivity of graphite foam are mainly empirical models [24], semi-analytical models [34] and analytical models [35–37]. For comparison, also included in Table 1 is the empirical model obtained by fitting the experimentally measured effective thermal conductivity of graphite foam [24]. Notably, a semi-analytical expression of effective thermal conductivity was obtained based upon a hexahedron UC with angular point and spherical holes [34]. Nonetheless, a major limitation of the model is that the involved empirical parameters vary with the porosity of graphite foam. Although Yu et al. [35], Leong and Li [36] and Chai et al. [37] also developed analytical solutions of effective thermal conductivity for graphite foams, the UCs adopted in their models were somewhat idealized and assumed to be periodically distributed, thus cannot accurately describe the randomness of pore size and distribution typically in graphite foams. In addition, the pore-scale behaviors of thermofluidic transport predicted by these models are different from the actual transport phenomena in porous media and hence need to be further exploited. It should also be pointed out that the UC has been extensively used to study heat conduction in graphite foams but rarely the permeability.

Existing studies paid little attention to studying and exploring pore-scale permeable flow and heat conduction in graphite foams with randomly distributed pore sizes and shapes. Fractal theory has an

excellent performance in characterizing the transport properties of porous media [38,39]. To address this issue, the current study aims to adopt the fractal theory [40] to describe the randomness of porous nature that inherently existed in graphite foams and develop analytical prediction models of permeability and conductivity. For validation, model predictions are compared with experimental and numerical simulation results. Besides, to provide in-depth analysis and insight into the mechanisms affecting permeability and effective conductivity, pore-scale numerical simulations on heat and fluid flow features are conducted by reconstructing the foam topology.

2. Analytical model of graphite foam

2.1. Theory of fractal porous media

The pore shape and pore size of a porous medium are often self-similar [41], following a fractal law, as shown in Fig. 1 for graphite foams having high porosities. To characterize the cumulative numbers of pores N and pore size of the porous medium with pore size equaling to or bigger than λ , the following fractal law has been developed [42]:

$$N(d \geq \lambda) = (\lambda_{\max}/\lambda)^{D_f} \quad (1)$$

where d denotes the length scale, λ_{\max} represents the maximum pore size, D_f is the fractal dimension of the porous medium. Here, $0 < D_f < 2$ and $0 < D_f < 3$ denote two- and three-dimensions, respectively. It has been established that the fractal dimension D_f takes the form of [43]:

$$D_f = d_E - \frac{\ln \varepsilon}{\ln(\lambda_{\min}/\lambda_{\max})} \quad (2)$$

where d_E is the Euclidean dimension, $d_E = 2$ or 3 denotes the two- or three-dimensional space, ε denotes the porosity, and λ_{\min} represents the minimum pore size.

The size distribution of pores in a porous medium is typically discrete and discontinuous. As shown in Fig. 1, the number of pores in a porous medium such as graphite foam is numerous. Thus, Eq. (1) can be viewed as a continuous and differentiable function. Upon taking differentiation on λ in Eq. (1) in an infinitesimal small range from λ to $\lambda + d\lambda$, one has [42]:

$$-dN = D_f \lambda_{\max}^{D_f} \lambda^{-(D_f+1)} d\lambda \quad (3)$$

where $-dN > 0$. For Eq. (1), the total number of pores N_t ranging from λ_{\min} to λ_{\max} is determined by Ref. [42]:

$$N_t = (\lambda_{\max}/\lambda_{\min})^{D_f} \quad (4)$$

Thus, dividing Eq. (3) by Eq. (4) leads to:

$$\frac{dN}{N_t} = D_f \lambda_{\min}^{D_f} \lambda^{-(D_f+1)} d\lambda = f(\lambda) d\lambda \quad (5)$$

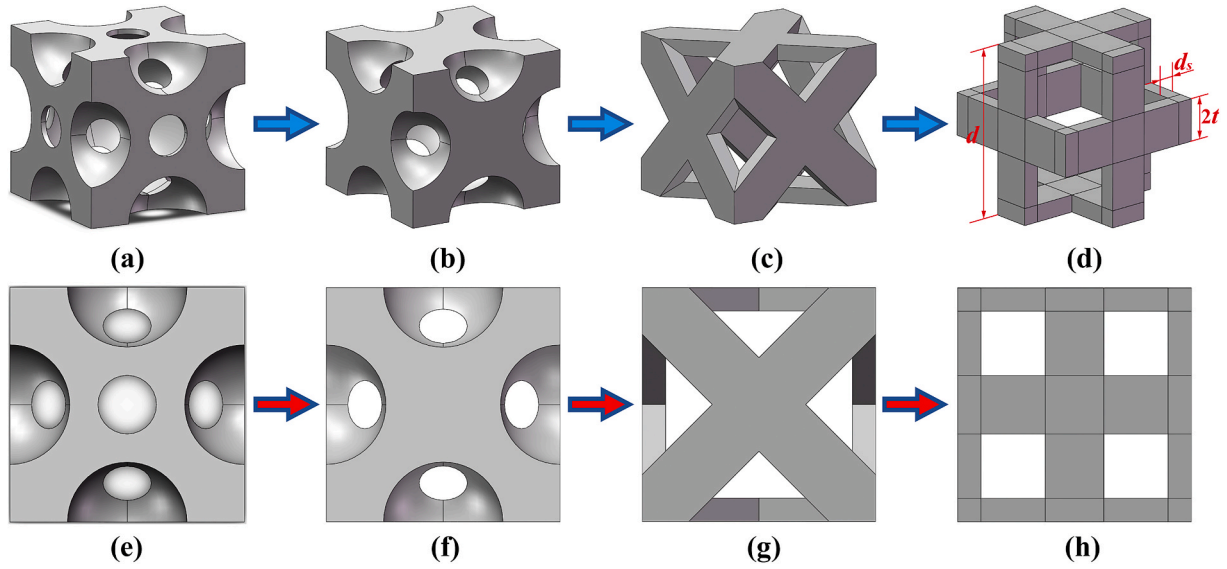


Fig. 2. Simplification process of representative structure (RS) for graphite foams: (a) 3D view of original RS (approximate pore structure; Fig. 1(c)); (b) 3D view of simplified transition model I; (c) 3D view of simplified transition model II; (d) 3D view of orthogonal-rod RS; (e) top view of approximate pore structure; (f) top view of simplified transition model I; (g) top view of simplified transition model II; (h) top view of orthogonal-rod RS.

where $f(\lambda) = D_f \lambda_{\min}^{D_f} \lambda^{-(D_f+1)}$ is the probability density function for pores in a fractal porous medium [42,43]. Based on the probability theory, the probability density function satisfies the following normalization condition [42,43]:

$$\int_{-\infty}^{+\infty} f(\lambda) d\lambda = \int_{\lambda_{\min}}^{\lambda_{\max}} f(\lambda) d\lambda = 1 - \left(\frac{\lambda_{\min}}{\lambda_{\max}}\right)^{D_f} \equiv 1 \quad (6)$$

when and only when

$$\left(\frac{\lambda_{\min}}{\lambda_{\max}}\right)^{D_f} \cong 0 \quad (7)$$

It follows that, when $\lambda_{\min} \ll \lambda_{\max}$ holds, the theory of fractal geometry can be used to calculate the basic properties (e.g., permeability and conductivity) of porous media [43].

The formulations detailed above pave the theoretical basis of fractal geometry describing the complex pore-scale morphologies of porous materials.

2.2. Permeability model

With the distribution and size of pores, as well as the tortuous tube-like pores in a porous medium assumed to satisfy the fractal law, it has been demonstrated that the generalized analytical model of permeability takes the form [42]:

$$K = \frac{\pi}{128} \frac{L_0^{1-D_f}}{A} \frac{D_f}{3 + D_f - D_f} \lambda_{\max}^{3+D_f} \quad (8)$$

where λ_{\max} is the maximum pore size, A and L_0 are separately the cross-sectional area of the cell in which the pore (with the cross-sectional area A_p) resides and the characteristic length corresponding to a set of fractal pores (including all fractal pores, regardless of pore sizes), and D_f denotes the fractal dimension for the average tortuosity.

Graphite foams are composed of many randomly-distributed spherical pores with different sizes, as shown in Fig. 1. Built upon the fractal models presented in the previous section, the cell cross-sectional area A (i.e., summation of pore cross-sectional and solid cross-sectional area in each cell) can be analytically expressed as [44–46]:

$$A = \frac{A_p}{\varepsilon} = - \int_{\lambda_{\min}}^{\lambda_{\max}} \frac{\pi}{\varepsilon} \left(\frac{\lambda}{2}\right)^2 dN = \frac{\pi D_{f,2} \lambda_{\max}^2 (1 - \varepsilon)}{4(2 - D_{f,2})\varepsilon} \quad (9)$$

where $D_{f,2} = 2 - \frac{\ln \varepsilon}{\ln(\lambda_{\min}/\lambda_{\max})}$ and A_p denotes the pore cross-sectional area.

Fig. 1(a) presents the scanning electron microscope (SEM) image of a representative graphite foam [24], from which it can be seen that the pores are not only randomly distributed but also have random sizes. At the same time, the shape of the pores is also self-similar. This provides the physical basis for using the fractal theory to characterize morphology of the graphite foam. Therefore, it is assumed that its pore distribution satisfies the pore-scale fractal law. It can be found in Fig. 1(a) that the pore shape of the graphite foam is close to spherical. Given simplicity, pores are treated as spherical and randomly distributed within a sufficiently large cubic cell. The pores of varying sizes penetrate each other, as displayed in Fig. 1(b). The shape of the pores is self-similar in the fractal hypothesis. Therefore, only one representative structure (RS) needs to be selected for theoretical modelling and numerical simulation. The RS shown in Fig. 1(c) is a self-similarity pore structure in the fractal distribution of the graphite foam, which approximates the random structure displayed in Fig. 1(a) and (b).

The RS of Fig. 1(c) still exhibits a complex structure, making theoretical analysis difficult to carry out. Therefore, to facilitate the analytical modeling of transport properties for graphite foams, its RS is further simplified to various extent, as depicted in Fig. 2. Firstly, its irregularly shaped ligaments are simplified as cuboids. Secondly, all the circular pores are treated as square pores. Finally, the diagonal ligaments are changed to ligaments that are connected at the midpoints of the opposite sides, as shown in Fig. 2. Note that these equivalent treatments are all based on the premise of equal porosity for the RS geometry. Eventually, the orthogonal-rod representative structure is obtained by simplification, as shown in Fig. 2(d).

With reference to Fig. 2(d), let d , d_s and $2t$ represent the length of the RS, the ligament thickness and the ligament width, in respective. When the pore of the RS is the maximum, the corresponding pore size is the maximum. In Fig. 2(d), the maximum pore size is related to its corresponding volume $V_{\max-p}$, as:

$$\lambda_{\max} = \sqrt[3]{V_{\max-p}} = \sqrt[3]{V_{l-p} - V_{s-p}} = \sqrt[3]{V_{s-p} \varepsilon / (1 - \varepsilon)} \quad (10)$$

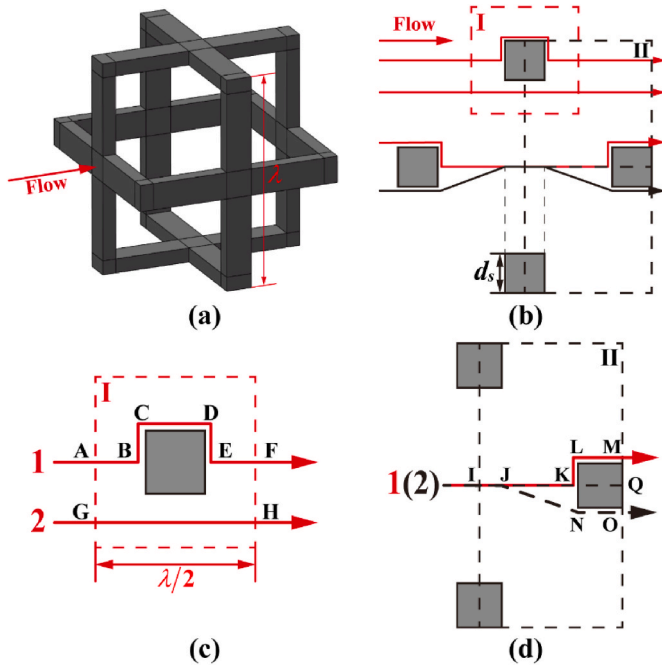


Fig. 3. Distribution of streamlines in the representative structure: (a) representative structure; (b) streamline distribution in simplified representative structure; (c) streamline distribution around a single ligament; (d) streamline distribution around a dislocated ligament.

where V_{t-p} and V_{s-p} are the total volume of the pore and the total volume of solid ligaments within the RS, respectively, with the latter calculated as:

$$V_{s-p} = 24td_s(d-t-d_s) \quad (11)$$

The fractal dimension D_T of average tortuosity is a key parameter in the generalized analytical model of fractal permeability presented in Eq. (8), given by Ref. [47]:

$$D_T = 1 + \frac{\ln \tau_{av}}{\ln(L_0/\lambda_{av})} \quad (12)$$

where λ_{av} and τ_{av} are separately the average pore diameter and the average tortuosity. When the pore-scale flow channels are approximately straight in a porous medium, $D_T = 1.0$. Once the parameters (λ_{av} , τ_{av} and L_0) in Eq. (12) are determined, D_T is finalized. The average pore diameter λ_{av} takes the form of [47]:

$$\lambda_{av} = \frac{D_{f,3}\lambda_{\min}}{D_{f,3} - 1} \quad (13)$$

while the characteristic length L_0 are given by Ref. [48]:

$$L_0 = \lambda_{\max} \left[\frac{\pi D_{f,3}}{6(3 - D_{f,3})} \frac{1 - \varepsilon}{\varepsilon} \right]^{\frac{1}{3}} \quad (14)$$

Here, ε is the porosity, $D_{f,3} = 3 - \frac{\ln \varepsilon}{\ln(\lambda_{\min}/\lambda_{\max})}$, λ_{\max} and λ_{\min} are the maximum and minimum pore size, respectively.

When λ_{av} and L_0 are determined, only the average tortuosity τ_{av} has not been determined in Eq. (12). The tortuosity of a porous medium is defined as the ratio of the actual tortuous flow path length to the straight (minimum) length [49]. However, typically, a porous medium contains many streamlines. Therefore, it is excessively difficult to calculate each tortuous path's tortuosity to obtain the average tortuosity. Nonetheless, it is confirmed that the average tortuosity can be evaluated by averaging the representative streamlines [50], thus making it possible to estimate the average tortuosity in a complex porous medium using the geometric

theory. The current study is mainly aimed at an isotropic open-cell graphite foam, for which the entrance direction of streamlines is depicted in Fig. 3(a). Solid ligaments in the foam are irregularly distributed because they contain many pores with random sizes. Accordingly, to further simplify the calculation, the ligaments of the simplified RS in Fig. 3(b) are employed to calculate the tortuosity as well as to simplify the irregularly distributed ligaments. Fig. 3(c) and (d) further reveal the distribution of streamlines near differently distributed ligaments: the former depicts the distribution near a single ligament while the latter shows the distribution near a dislocated ligament.

In the current study, the average tortuosity τ_{av} is estimated by the weight analysis average of all possible flow streamlines detouring the struts in the RS (see Fig. 3(b)), as:

$$\tau_{av} = \sum_{i=1}^n a_i \tau_i \quad (15)$$

where a is the weight value, with the sum of all weighted values equaling to one ($\sum_{i=1}^n a_i = 1$), τ_i is the local tortuosity corresponding to the i -th flow streamline, and n denotes the total number of streamlines. In particular, when all the weights are equal ($a_1 = a_2 = \dots = a_n$), Eq. (15) becomes a statistical average [50]. Given that a good deal of flow paths is contained in an RS, it seems unacceptable to calculate all the streamlines to obtain the average tortuosity. It has been proposed that τ_{av} is mainly affected by the longest and the shortest tortuosity in a RS [50].

Fig. 3(c) and (d) demonstrate two representative distributions of streamlines in the cubic RS with a size of λ . With the size of each solid strut denoted as d_s , the pore volume of the cell I (or II) in Fig. 3(c) and (d) can be readily calculated by:

$$V_{RS-pore} = \left(\frac{\lambda}{2}\right)^2 \lambda - \lambda \cdot d_s^2 \quad (16)$$

while the total volume of cell I (or II) is:

$$V_{RS-total} = \lambda \left(\frac{\lambda}{2}\right)^2 \quad (17)$$

Therefore, for cell I (or II) in Fig. 3(c) and (d), the porosity can be calculated by:

$$\varepsilon = \frac{V_{RS-pore}}{V_{RS-total}} = 1 - 4 \left(\frac{d_s}{\lambda}\right)^2 \quad (18)$$

It follows that:

$$\frac{d_s}{\lambda} = \frac{1}{2} \sqrt{1 - \varepsilon} \quad (19)$$

For streamline 1 in Fig. 3(c), $l_{AB} = l_{EF} = \frac{\lambda}{2} - d_s$, $l_{BC} = l_{DE} = \frac{d_s}{2}$, and $l_{CD} = d_s$. Based on the tortuosity definition, the tortuosity of streamline 1 in Fig. 3(c) can be expressed as:

$$\tau_{1-1} = \frac{l_{AB} + l_{BC} + l_{CD} + l_{DE} + l_{EF}}{l_{AB} + l_{CD} + l_{EF}} = 1 + 2 \frac{d_s}{\lambda} = 1 + \sqrt{1 - \varepsilon} \quad (20)$$

For streamline 2 illustrated in Fig. 3(c), the actual length l_{GH} and the straight length of flow path l_{GH} are equal, and hence its tortuosity is simply:

$$\tau_{1-2} = \frac{l_{GH}}{l_{GH}} = 1 \quad (21)$$

In Fig. 3(c), the streamline is tortuous near the ligament but almost straight further away from it. As porosity decreasing, the volume of ligaments in the RS increases, causing more tortuous streamlines. The two weight for streamlines 1 and 2 in Fig. 3(c) are $a_{1-1} = \frac{\lambda d_s^2}{\lambda(\lambda/2)^2} = 4 \left(\frac{d_s}{\lambda}\right)^2$ and $a_{1-2} = \frac{\lambda(\lambda/2)^2 - \lambda d_s^2}{\lambda(\lambda/2)^2} = 1 - 4 \left(\frac{d_s}{\lambda}\right)^2$, in respective. Hence, the average tortuosity τ_1 in Fig. 3(c) can be achieved as:

$$\tau_1 = a_{1-1}\tau_{1-1} + a_{1-2}\tau_{1-2} = 4\left(\frac{d_s}{\lambda}\right)^2 \tau_{1-1} + \left[1 - 4\left(\frac{d_s}{\lambda}\right)^2\right] \tau_{1-2} = 1 + (1-\varepsilon)\sqrt{1-\varepsilon} \quad (22)$$

For streamline 1 in Fig. 3(d), $l_{IJ} = l_{KL} = \frac{d_s}{2}$, $l_{JK} = \frac{\lambda - 3d_s}{2}$ and $l_{LM} = l_{KQ} = d_s$. Its tortuosity can thence be obtained as:

$$\tau_{2-1} = \frac{l_{IJ} + l_{JK} + l_{KL} + l_{LM}}{l_{IJ} + l_{JK} + l_{KQ}} = 1 + \frac{d_s}{\lambda} = 1 + \frac{\sqrt{1-\varepsilon}}{2} \quad (23)$$

Similarly, for streamline 2 in Fig. 3(d), as $l_{NO} = d_s$ and $l_{JN} = \sqrt{l_{JK}^2 + l_{KN}^2} = \sqrt{\left(\frac{\lambda}{2} - \frac{3d_s}{2}\right)^2 + \left(\frac{d_s}{2}\right)^2}$, its tortuosity is determined by:

$$\tau_{2-2} = \frac{l_{IJ} + l_{JN} + l_{NO}}{l_{IJ} + l_{JK} + l_{KQ}} = 3\frac{d_s}{\lambda} + \sqrt{\left(1 - 3\frac{d_s}{\lambda}\right)^2 + \left(\frac{d_s}{\lambda}\right)^2} = \frac{3}{2}\sqrt{1-\varepsilon} + \frac{1}{2}\sqrt{14 - 10\varepsilon - 12\sqrt{1-\varepsilon}} \quad (24)$$

For the strut topology shown in Fig. 3(d), the ratio of streamline 1 to 2 is not influenced via porosity. Streamlines 1 and 2 are equally likely to occur, regardless of the porosity variation in Fig. 3(d). Thus, they take the same weight for tortuous flow, e.g., $a_{2-1} = a_{2-2} = \frac{1}{2}$, yielding:

$$\tau_{2-2} = a_{2-1}\tau_{2-1} + a_{2-2}\tau_{2-2} = \frac{1}{2}\tau_{2-1} + \frac{1}{2}\tau_{2-2} = \frac{2 + 4\sqrt{1-\varepsilon} + \sqrt{14 - 10\varepsilon - 12\sqrt{1-\varepsilon}}}{4} \quad (25)$$

where a_{2-1} and a_{2-2} are the weight value for streamlines 1 and 2, respectively.

In a real porous medium like the graphite foam, the pores often have a random distribution in size and shape and the corresponding solid ligaments are irregular. Therefore, it is difficult to measure experimentally the proportions of the two ligament distributions in Fig. 3(c) and (d). In the present study, for simplicity, the analysis on tortuosity detailed above is accepted for the cases shown in Fig. 3(c) and (d), i.e., $a_1 = a_2 = \frac{1}{2}$. Here, a_1 is the weight value for the dislocated and equidistant arrangement in Fig. 3(c), and a_2 is the weight value for the square configuration in Fig. 3(d). Then, based on Eqs. (22) and (25), the average tortuosity is manipulated to be:

$$\tau_{av} = a_1\tau_1 + a_2\tau_2 = \frac{1}{2}\tau_1 + \frac{1}{2}\tau_2 = \frac{6 + (8 - 4\varepsilon)\sqrt{1-\varepsilon} + \sqrt{14 - 10\varepsilon - 12\sqrt{1-\varepsilon}}}{8} \quad (26)$$

For Eq. (12), the parameters λ_{av} , L_0 and τ_{av} are all determined by Eqs. (13), (14) and (26). Therefore, the fractal dimension D_T of τ_{av} is also determined.

Eventually, as the required parameters are determined, the permeability of a graphite foam can be explicitly expressed as:

$$\frac{K}{d_s^2} = \frac{1}{32} \frac{D_{f,3}(2 - D_{f,2})}{D_{f,2}(3 + D_T - D_{f,3})} \left[\frac{\pi D_{f,3}}{6(3 - D_{f,3})} \frac{1 - \varepsilon}{\varepsilon} \right]^{\frac{1-D_T}{3}} \left[24\frac{\zeta}{\gamma} \left(\frac{1}{\gamma} - \frac{\zeta}{\gamma} - 1 \right) \frac{\varepsilon}{1-\varepsilon} \right]^{\frac{2}{3}} \frac{\varepsilon}{1-\varepsilon} \quad (27)$$

where $\gamma = d_s/d$ and $\zeta = t/d$.

2.3. Effective thermal conductivity model

Thermal conductivity of graphite foam is analyzed using a combination of the fractal theory and the thermal-electrical analogy. To this end, the fractal morphology of the foam is described using the approach introduced by Yu and Cheng [51] for granular porous media. As shown schematically in Fig. 4(a), Yu and Cheng [51] regarded a granular porous medium as composed of curved granular chains. Built upon this approach, to model heat conduction in graphite foam, the original granule in the granular chains is replaced by a RS representing the

graphite foam, as shown in Fig. 4(b). Then, for predicting conductivity, the following steps are undertaken sequentially:

- 1) Calculate thermal resistance of individual RS;
- 2) Calculate thermal resistance of a RS chain composed of RSs in series;
- 3) Calculate the effective thermal conductivity of graphite foam composed of different RS chains in parallel.

2.3.1. Thermal resistance of representative structure (RS)

Upon considering the symmetry of the RS as shown in Fig. 5(a), a one-eighth cell is selected to analyze its thermal resistance, with its top section subjected to constant heat flow. Since the parent material of graphite foam has a very high thermal conductivity, the foam exhibits a large conductivity ratio of solid ligament (k_s) to filling fluid (k_f): for instance, when saturated with air, the ratio is as high as 30188–75471. Therefore, heat conduction mainly exists along the z -axis direction in parallel, and only the thermal resistance along the thermal flow direction needs to be considered. In addition, the thermal contact resistance of graphite ligaments as well as convection and thermal radiation in the RS are ignored during the analysis of effective conductivity.

With reference to Fig. 5(b), let d_s , $2t$ and d denote the thickness of ligament, width of ligament and pore size, respectively. The one eighth of the RS can be divided into three layers (i.e., A, B and C) from left to right (i.e., the x -axis direction). The A-layer can be further subdivided into three sublayers (i.e., A1, A2 and A3), and their thermal resistances can be calculated as:

$$R_{A1} = \frac{d}{2k_s d_s t} \quad (28)$$

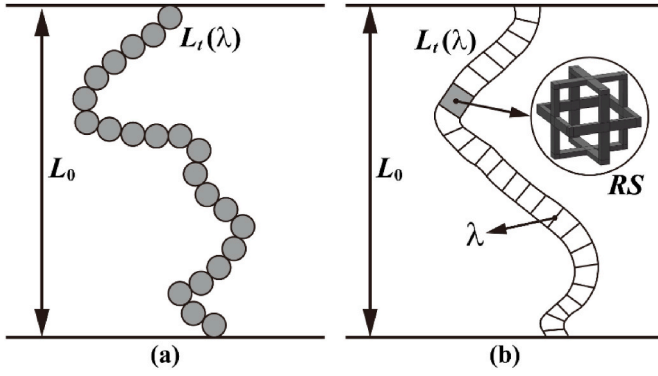


Fig. 4. Schematic demonstration of thermal path in porous media: (a) granular chain in granular porous media [51]; (b) RS chain in graphite foams.

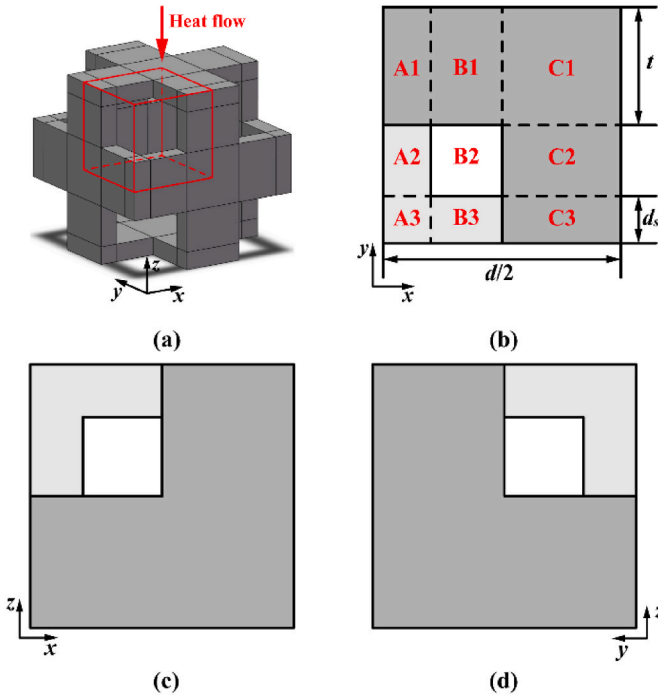


Fig. 5. Schematic of representative structure thermal resistance: (a) representative structure; (b) top, (c) front and (d) side view.

$$R_{A2} = \frac{d-2t}{k_f d_s (d-2t-2d_s)} + \frac{2t}{k_s d_s (d-2t-2d_s)} \quad (29)$$

$$R_{A3} = \frac{d-2t}{2k_f d_s^2} + \frac{t}{k_s d_s^2} \quad (30)$$

The A-layer thermal resistance is obtained by connecting the A1, A2 and A3 sublayers in parallel, as:

$$\frac{1}{R_A} = \frac{1}{R_{A1}} + \frac{1}{R_{A2}} + \frac{1}{R_{A3}} = \frac{2k_s d_s t}{d} + \frac{k_s k_f d_s (d-2t)}{k_s (d-2t) + 2k_f t} \quad (31)$$

Similarly, the thermal resistance of the B-layer composed of B1, B2 and B3 sublayers in parallel is calculated as:

$$R_{B1} = \frac{2d_s}{k_s t (d-2t-2d_s)} + \frac{d-2d_s}{k_f t (d-2t-2d_s)} \quad (32)$$

$$R_{B2} = \frac{2d}{k_f (d-2t-2d_s)^2} \quad (33)$$

$$R_{B3} = \frac{d-2t}{k_f d_s (d-2t-2d_s)} + \frac{2t}{k_s d_s (d-2t-2d_s)} \quad (34)$$

$$\frac{1}{R_B} = \frac{1}{R_{B1}} + \frac{1}{R_{B2}} + \frac{1}{R_{B3}} = \frac{k_s k_f t (d-2t-2d_s)}{2k_f d_s + k_s (d-2d_s)} + \quad (35)$$

$$\frac{k_f (d-2t-2d_s)^2}{2d} + \frac{k_s k_f d_s (d-2t-2d_s)}{k_s (d-2t) + 2k_f t}$$

As noticed in Fig. 5(b), the thermal resistances of the C1, C2 and C3 sublayers are connected in parallel to construct the C-layer thermal resistance. Then, the C-layer thermal resistance can be calculated as:

$$\frac{1}{R_C} = \frac{1}{R_{C1}} + \frac{1}{R_{C2}} + \frac{1}{R_{C3}} = \frac{k_s k_f t (d-2d_s)}{2k_f d_s + k_s (d-2d_s)} + \frac{2k_s t d_s}{d} \quad (36)$$

where

$$R_{C1} = \frac{d_s}{k_s t^2} + \frac{d-2d_s}{2k_f t^2} \quad (37)$$

$$R_{C2} = \frac{2d_s}{k_s t (d-2t-2d_s)} + \frac{d-2d_s}{k_f t (d-2t-2d_s)} \quad (38)$$

$$R_{C3} = \frac{d}{2k_s t d_s} \quad (39)$$

Upon paralleling layers A, B, and C, the thermal resistance of the one-eighth RS in Fig. 5(b) is calculated as:

$$\frac{1}{R_{one-eighth-RS}} = \frac{1}{R_A} + \frac{1}{R_B} + \frac{1}{R_C} = \frac{4k_s d_s t}{d} + \frac{k_f (d-2t-2d_s)^2}{2d} + \frac{2k_s k_f d_s (d-2t-d_s)}{2k_f t + k_s (d-2t)} + \frac{2k_s k_f t (d-t-2d_s)}{2k_f d_s + k_s (d-2d_s)} \quad (40)$$

Eventually, the total thermal resistance of the RS is obtained as:

$$\frac{1}{R_{RS}} = \frac{2}{R_{one-eighth-RS}} = d\beta \quad (41)$$

where

$$\beta = 8k_s \gamma \zeta + k_f (1-2\zeta-2\gamma)^2 + \frac{4k_s k_f \gamma (1-2\zeta-\gamma)}{2k_f \zeta + k_s (1-2\zeta)} + \frac{4k_s k_f \zeta (1-\zeta-2\gamma)}{2k_f \gamma + k_s (1-2\gamma)} \quad (42)$$

2.3.2. RS chain model

Previously, a granular porous medium consisted of non-contacting and curved granular chains [51], as shown in Fig. 4(b). Based on this concept, the graphite foam of concern is assumed to be composed of RS chains with different pore sizes. Then, for the idealized foam topology of Fig. 5(a), a tortuous RS chain is formed by a series of RSs having identical pore size, as shown in Fig. 4(b). Further, the graphite foam is composed of tortuous RS chains having different pore sizes in parallel, and the RS chains are assumed to obey the fractal distribution law. Subsequently, the effective thermal conductivity is obtained in two steps. The effective conductivity of a single RS chain is first derived using a series model. Then, the effective conductivity of graphite foam composed of multiple RS chains with different pore sizes is derived using a parallel model.

The actual length (L_t) of a fluid passing through a porous medium with pore size λ satisfies the fractal law [42]:

$$L_t(\lambda) = \lambda^{1-D_f} L_0^{D_f} \quad (43)$$

In the current study of graphite foam, the flow of heat along a single RS chain with pore size λ is assumed to have a heat conduction actual length $L_t(\lambda)$, in which the number of RSs is $L_t(\lambda)/\lambda$. Fourier's law then dictates that the thermal resistance of a single tortuous RS chain is:

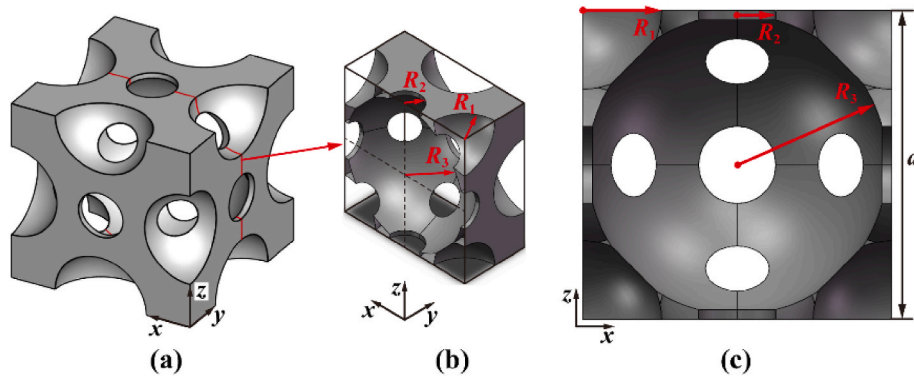


Fig. 6. Schematic of geometric structure parameters for the numerical simulation model of graphite foam: (a) solid phase; (b) cross-section diagram; (c) main view of a cross-sectional diagram.

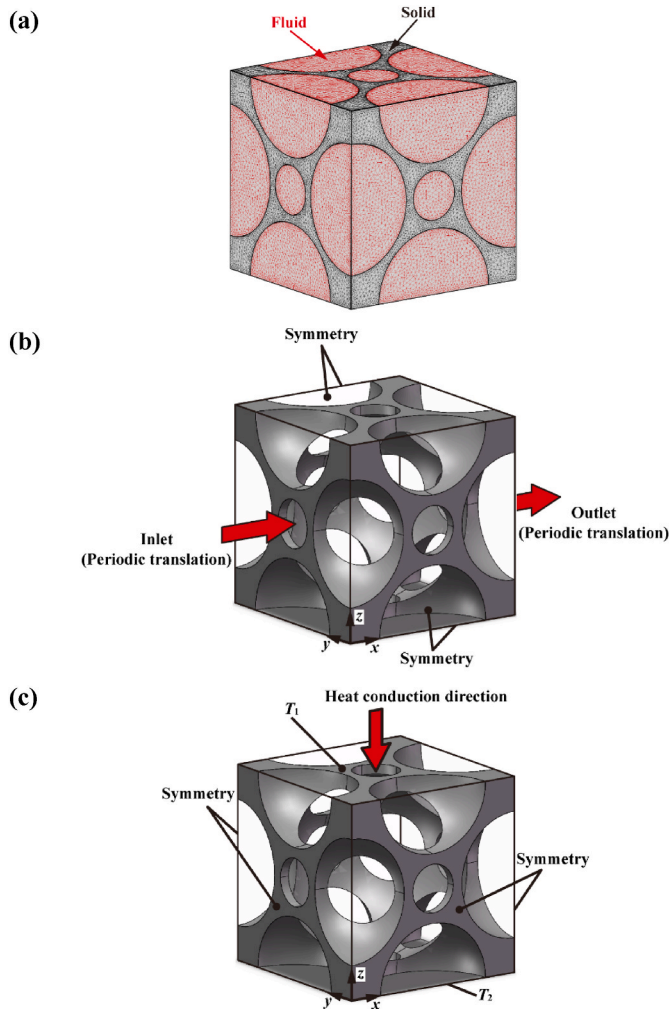


Fig. 7. Computational domain and boundary conditions: (a) representative mesh; (b) boundary conditions for permeability; (c) boundary conditions for effective thermal conductivity.

Table 2
Results of grid independence test.

Foam specimen	Grid 1	Grid 2	Grid 3	Grid 4
	297085	895789	1959090	4365895
Pressure drop ΔP (Pa)				
GF-1	4.86×10^{-4}	5.08×10^{-4}	5.92×10^{-4}	6.03×10^{-4}
Difference	19.4%	15.8%	1.8%	Baseline
Heat flux (W/m^2)				
GF-1	502554	501857	501048	500796
Difference	0.35%	0.21%	0.05%	Baseline

Table 3
Parent and filling materials of graphite foams for effective thermal conductivity simulation.

Materials	k_s (W/(m·K))	Materials	k_s (W/(m·K))
ORNL GF [24]	1300	Pure CF [52]	3.5
ARA24-D foam (1000 °C)	0.25–25 (~14)	UGF [53]	330–740 (~535)
ARA24-D foam (2800 °C)	~1150	Air	0.0267
POCO foam™ [24]	1640	Paraffin wax [53]	0.28

Note: ^a “GF”, “CF” and “UGF” represent graphite foam, carbon foam and ultra-thin graphite foam, respectively.

Table 4
Pore-scale geometric parameters.

Foam sample	ϵ	a (mm)	R_1 (μm)	R_2 (μm)	R_3 (μm)	d_s (μm)
GF-1	0.686	0.4	102	50	194	96
GF-2	0.709	0.4	100	40	200	86
GF-3	0.732	0.4	110	50	195	77
GF-4	0.749	0.4	115	52	192.6	70
GF-5	0.767	0.4	120	50	190	64
GF-6	0.783	0.4	122.6	50	190	59
GF-7	0.798	0.4	125	50	190	54
GF-8	0.813	0.4	129	50	187	49
GF-9	0.835	0.4	133	50	185	42
GF-10	0.852	0.4	136	50	183	37
GF-11	0.876	0.4	140	50	180	31
GF-12	0.892	0.4	150	24	160	26
GF-13	0.918	0.4	150	32	170	20

Note: ^a “Sim” represents simulate data, and d_s is calculated by Eq. (47) where $\zeta = 0.08$.

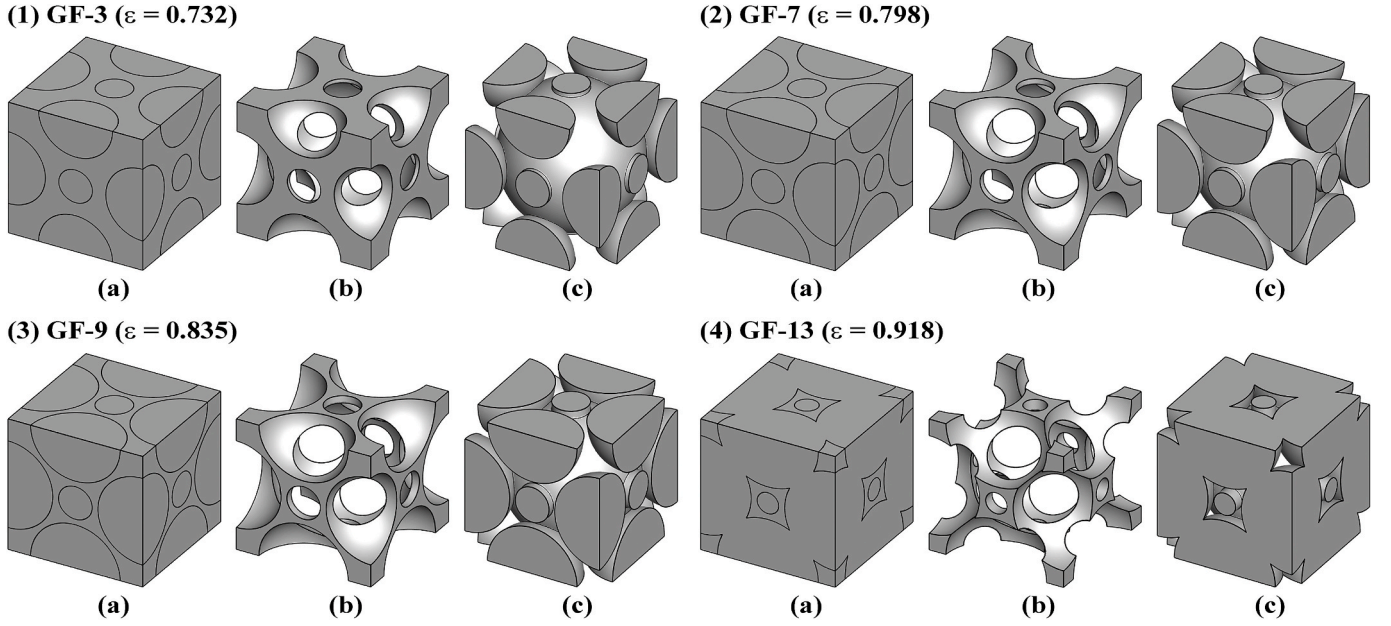


Fig. 8. Direct numerical simulation models with varying porosities: (a) graphite foam assembly; (b) solid phase; (c) fluid phase.

Table 5

Comparison between predictions of fractal permeability model and existing experimental measurements for graphite foams.

Foam sample	ε	λ (μm)	d_s (μm)	ζ	K (Exp) (m^2)	K (Pre) (m^2)	RD (%)
Leong et al. [54]	0.75	310	110 ^a	0.058	7.74×10^{-10}	7.78×10^{-10}	0.52
Straatman et al. [55]	0.82	500	82.3 ^b	0.044	6.13×10^{-10}	6.17×10^{-10}	0.65

Note.

^a Estimated from the scanning electron microscope (SEM) image in Leong et al. [54].

^b Calculated based on empirical correlation [56]: $\frac{d_s}{d_p} = 1.18 \sqrt{\frac{1-\varepsilon}{3\pi} \left(\frac{1}{1-e^{-(1-\varepsilon)/0.04}} \right)}$.

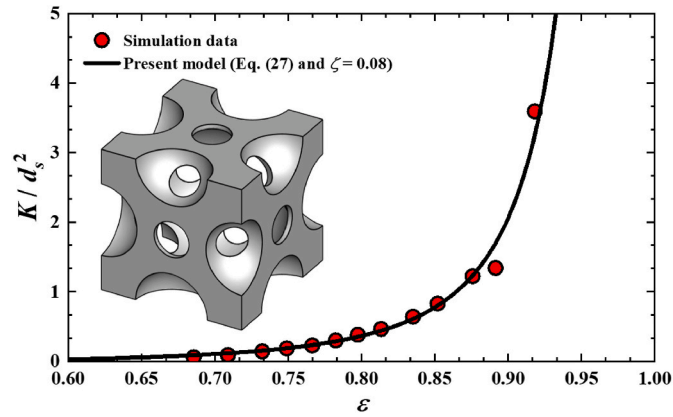


Fig. 9. Comparison between theoretical model predictions and numerical simulation results.

$$R_{chain} = \frac{L_t(\lambda)}{\lambda} R_{RS} = \frac{\lambda^{-1-D_f} L_0^{D_f}}{1+2\gamma} \beta^{-1} \quad (44)$$

From Eq. (3), the number of tortuous chains is $-dN = D_f \lambda^{D_f} \lambda^{-(D_f+1)} d\lambda$ within the infinitesimal range of λ to $\lambda + d\lambda$ for pore sizes. Thus, with these chains taken as connected in parallel, the total thermal resistance of the graphite foam is finalized as:

$$\frac{1}{R_t} = \int_{\lambda_{min}}^{\lambda_{max}} \frac{D_f \lambda^{D_f} \lambda^{-(D_f+1)} d\lambda}{R_{chain}} \quad (45)$$

2.3.3. Effective thermal conductivity

According to Eqs. (9), (14) and (45), the effective conductivity of the graphite foam can be obtained as:

$$k_e = \frac{L_0}{AR_t} = \frac{(1+2\gamma)(2-D_{f,2})\varepsilon}{(D_T-D_{f,2}+1)(1-\varepsilon)} \left[\frac{\pi D_{f,3}(1-\varepsilon)}{6(3-D_{f,3})\varepsilon} \right]^{\frac{1-D_f}{3}} \left(1 - \varepsilon^{\frac{D_f-D_{f,2}+1}{2-D_{f,2}}} \right) \beta \quad (46)$$

where β is determined by Eq. (42). From Fig. 5(a), the porosity ε can be expressed as:

$$\varepsilon = 1 - \frac{V_s}{V_{RS}} = 1 - 24\zeta\gamma(1-\zeta-\gamma) \quad (47)$$

where $\gamma = d_s/d$, $\zeta = t/d$ and $0 < \gamma + \zeta < 0.5$. The dimensionless numbers are related to the structural parameters (d , d_s , and t). For different porous materials, the value of ζ may be different. When the dimensionless number ζ is determined, the dimensionless number γ and the porosity ε are in a one-to-one correspondence by Eq. (47). The structural parameters in Fig. 2(d) are simplified models of complex graphite foams. These structural parameters are difficult to measure based on experiments, and many experimental data also lacks these parameters. But these parameters have actual physical meanings. However, precisely determining these parameters needs to be further studied in the future.

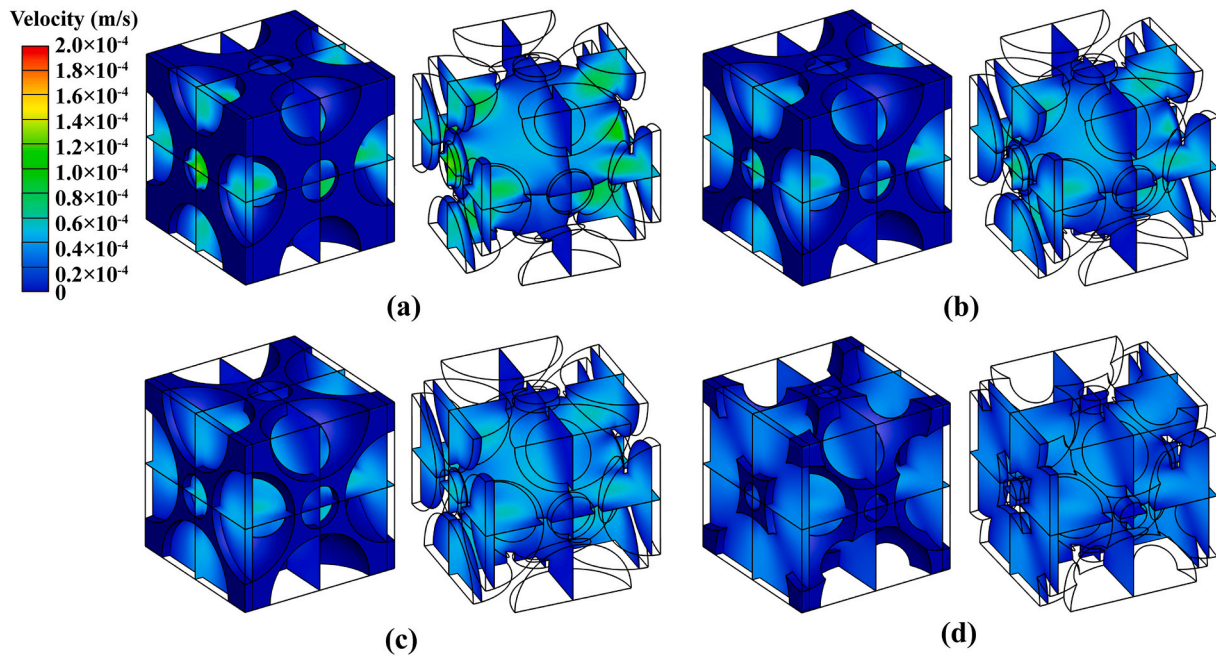


Fig. 10. Velocity field in graphite foam cells having various porosities: (a) GF-3; (b) GF-7; (c) GF-9; (d) GF-13.

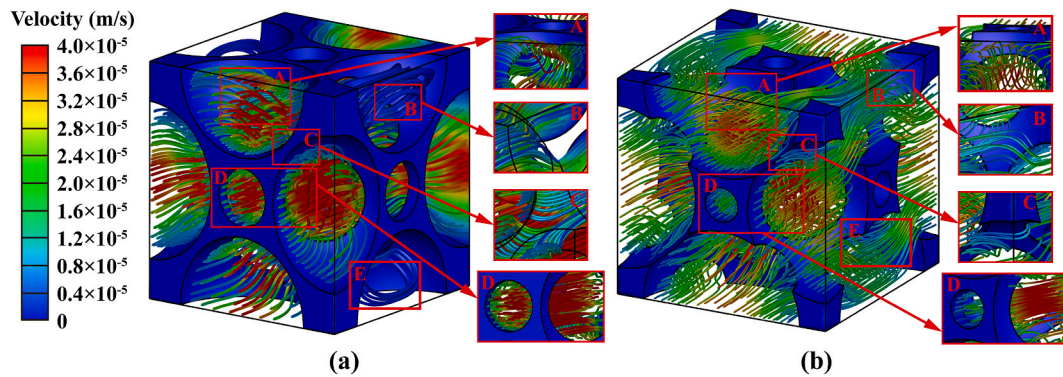


Fig. 11. Streamline distribution: (a) GF-9; (b) GF-13.

3. Pore-scale numerical simulation

3.1. Problem setup

The commercial software ANSYS CFX 19.1 is employed to simulate both pore-scale permeable flow and conduction in graphite foams as well as explore the underlying transport mechanisms.

To perform the pore-scale direct numerical simulations, quantifying the effect of local ligaments on flow and heat conduction behaviours is of vital importance. According to SEM images of graphite foam (e.g., Fig. 1 (a)), the numerically simulated cubic unit pore structure for graphite foam is selected, with its solid geometry shown in Fig. 6(a). In Fig. 6(b) and (c), for the simplified foam solid geometry, the pores on each prong are quarter spheres of radius R_1 , the pores on each surface are circles of radius R_2 , the central pore is a sphere of radius R_3 , and the side length of the cubic model is a .

It is difficult to use structured meshes to model the foam structures. The commercial software ANSYS ICEM CFD 19.1 is adopted to generate unstructured tetrahedral meshes, as shown in Fig. 7(a), with appropriate densification at fluid-solid contact surfaces. For grid independence checking, four sets of meshes with different elements (297085, 895789, 1959090, and 4365895) are applied, and the results are demonstrated in

Table 2. Predicted values for pressure drop and heat flux remain almost unchanged once the grid number exceeds 1.95 million: as the grid number is increased from 1959090 to 4365895, the pressure drop change is less than 2% while the heat flux change is less than 0.1%. Therefore, the number of mesh elements is no less than 1959090 in subsequent simulations.

3.2. Permeability modelling

To numerically calculate the foam permeability, the boundary conditions adopted are displayed in Fig. 7(b): two faces are set as the inlet and outlet for air flow, and the other four faces are symmetric. To obtain stable and fully developed flow inside the pore-scale model, a periodic translational boundary condition with a mass flow rate of $3.13 \times 10^{-12} \text{ kg}\cdot\text{s}^{-1}$ is applied. Since the Reynolds number (based on cell size) is calculated to be less than 1.0, the effect of fluid inertial force can be disregarded. To ensure the accuracy of the present numerical simulations, the convergence residuals for both continuity and momentum equations in every iteration are less than 10^{-7} .

Table 6
Experimental data of effective thermal conductivity for graphite foams filled by air or paraffin.

References	Bulk density (g/cm ³)	Ligament density (g/cm ³)	Porosity, ϵ	k_e (W/(m·K))	Remarks
Klett et al. [24]	0.6192	2.23	0.7223 ^a	151.87	ORNL GF-Air
	0.6096	2.23	0.7267 ^a	160.16	
	0.6086	2.23	0.7271 ^a	169.23	
	0.5991	2.23	0.7314 ^a	131.76	
	0.5990	2.23	0.7314 ^a	149.90	
	0.5989	2.23	0.7314 ^a	160.95	
	0.5894	2.23	0.7357 ^a	151.48	
	0.5691	2.23	0.7448 ^a	148.72	
	0.5393	2.23	0.7581 ^a	127.81	
	0.4797	2.23	0.7849 ^a	104.54	
	0.4690	2.23	0.7897 ^a	119.92	
	0.4499	2.23	0.7983 ^a	86.79	
	0.4007	2.23	0.8203 ^a	74.95	
	0.3902	2.23	0.8250 ^a	68.24	
	0.3901	2.23	0.8251 ^a	74.56	
	0.3794	2.23	0.8298 ^a	92.31	
	0.3102	2.23	0.8609 ^a	55.23	
	0.2996	2.23	0.8656 ^a	52.47	
	0.2899	2.23	0.8700 ^a	67.06	
	0.2803	2.23	0.8743 ^a	61.54	
0.2697	2.23	0.8790 ^a	48.13		
0.2504	2.23	0.8877 ^a	50.49		
Fleming et al. [53]	0.188	N/A	0.916	16.5	UGF-Paraffin wax
	0.166	N/A	0.925	14	
	0.131	N/A	0.941	13.7	
	0.088	N/A	0.96	7.1	
	0.076	N/A	0.966	7.6	
	0.048	N/A	0.978	2.6	
	0.019	N/A	0.9913	2.4	
Klett et al. [24]	N/A	N/A	0.73	182	POCO Foam TM -Air
Straatman et al. [55]	N/A	N/A	0.82	120	
Jana et al. [52]	0.280 ^b	1.934	0.8551	0.151	Pure CF-Air
	0.170 ^b	1.934	0.9123	0.099	
	0.13	1.934	0.933	0.11	
	0.080 ^b	1.934	0.9585	0.061	
	0.065 ^b	1.934	0.9662	0.052	
	0.058 ^b	1.934	0.9700	0.048	
	0.045 ^b	1.934	0.9766	0.039	
Klett et al. [20]	0.579	2.06	0.7189 ^a	1.201	ARA24-D Foam (1000 °C)-Air
	0.540	2.06	0.7381 ^a	1.701	
	0.530	2.06	0.7428 ^a	1.601	
	0.439	2.06	0.7867 ^a	1.303	
	0.420	2.06	0.7962 ^a	1.104	
	0.410	2.06	0.8010 ^a	1.104	
	0.369	2.06	0.8206 ^a	1.203	
	0.360	2.06	0.8253 ^a	1.000	
	0.240	2.06	0.8836 ^a	0.701	
	0.230	2.06	0.8883 ^a	0.602	
	0.230	2.06	0.8883 ^a	0.701	
	0.220	2.06	0.8931 ^a	0.602	
	Klett et al. [20]	0.589	2.23	0.7357 ^a	
0.570		2.23	0.7446 ^a	148.8	
0.549		2.23	0.7540 ^a	85.6	
0.539		2.23	0.7584 ^a	128.0	
0.480		2.23	0.7848 ^a	104.8	
0.400		2.23	0.8207 ^a	75.0	
0.389		2.23	0.8257 ^a	68.1	
0.389		2.23	0.8257 ^a	74.7	
0.379		2.23	0.8301 ^a	92.3	
0.310		2.23	0.8610 ^a	55.3	
0.299		2.23	0.8659 ^a	52.8	
0.289		2.23	0.8704 ^a	67.3	
0.279		2.23	0.8748 ^a	62.1	
0.269		2.23	0.8792 ^a	48.3	
0.250		2.23	0.8880 ^a	50.7	

Note.

^a $\epsilon = 1 - \rho_{\text{bulk}}/\rho_{\text{ligament}}$, where ρ_{bulk} and ρ_{ligament} are bulk density and ligament density, respectively.

^b $\rho_{\text{bulk}} = \rho_{\text{ligament}}(1 - \epsilon)$.

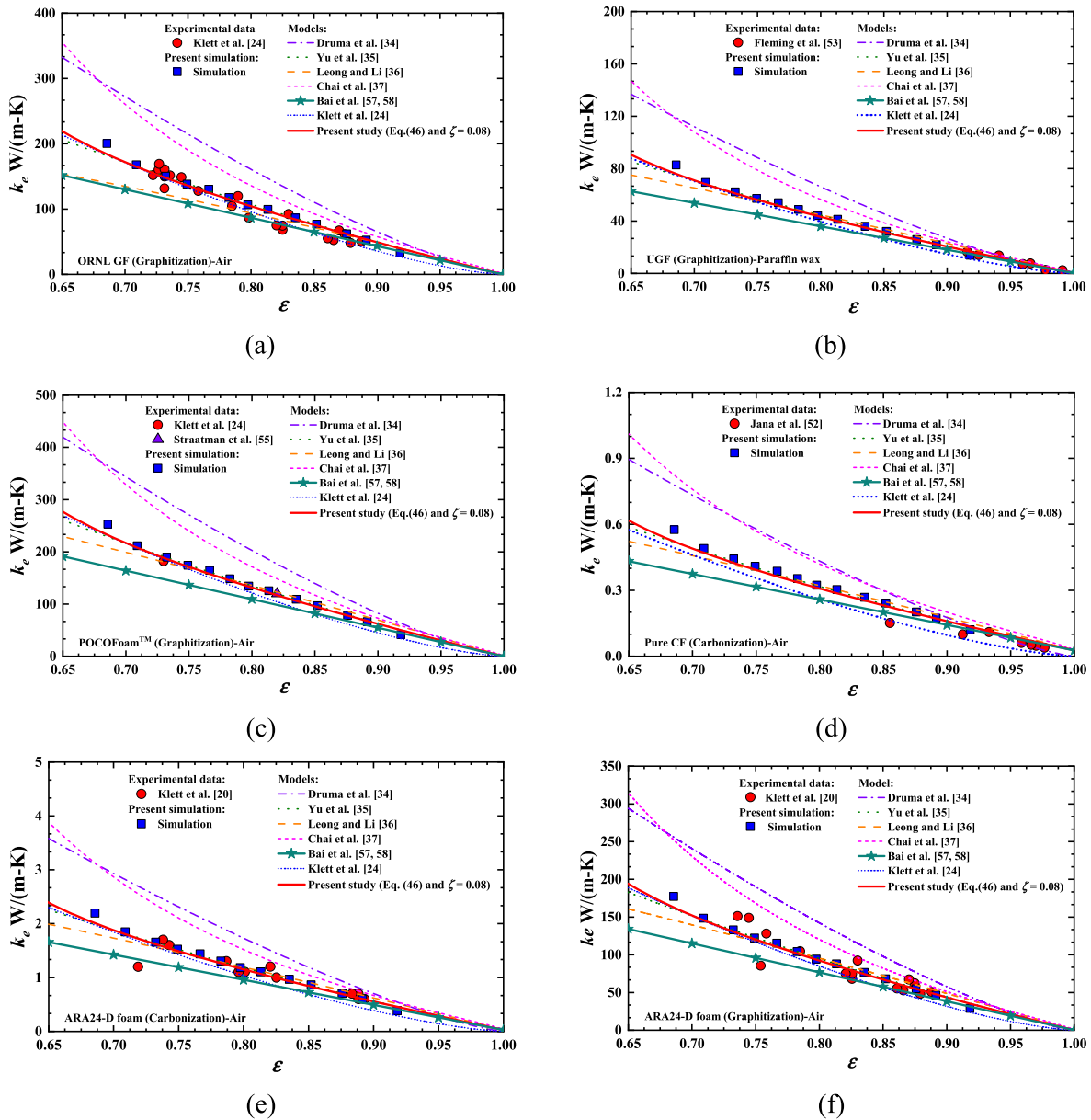


Fig. 12. Comparisons among model predictions, experimental data and simulation data: (a) ORNL GF-Air; (b) UGF-Paraffin wax; (c) POCO foam™-Air; (d) Pure CF-Air; (e) ARA24-D foam (1000 °C)-Air; (f) ARA24-D foam (2800 °C)-Air.

3.3. Effective thermal conductivity modelling

Owing to the fact that the parent material of a graphite foam varies significantly from one manufacturer to another due to difference in processing routines, thus has notably effect on its effective thermal conductivity. For the present pore-scale numerical simulations of effective conductivity, the thermal conductivities of different parent materials and filling substrates are shown in Table 3. The boundary conditions adopted for these simulations are presented in Fig. 7(c): the top surface temperature is fixed at 300 K (i.e., $T_1 = 300$ K), the bottom surface temperature is set at 299 K (i.e., $T_2 = 299$ K), while the remaining four faces are symmetric. It has been demonstrated that energy equations convergence criteria in each iteration set at 10^{-10} ensure the calculation accuracy.

3.4. Pore-scale simulation models of varying porosities

To provide in-depth transport characteristics in a graphite foam and calculate its effective thermal conductivity and permeability, numerical simulations are performed with a series of pore-scale geometry models, with the porosity varied from 0.686 to 0.918. Table 4 summarizes relevant pore-scale geometrical parameters of the foam. For the calculation, the foam porosity is varied from 0.686 to 0.918 (i.e., $0.686 \leq \epsilon \leq 0.918$). In respective, selected geometry models are presented in Fig. 8 with respect to graphite foam assembly, solid phase, and fluid phase. The overall size of computational domain (i.e., the cubic cell) is fixed as the porosity is varied, as illustrated in Fig. 8(a). Varying the porosity leads to variations in ligament thickness and shape (Fig. 8(b)): the higher the porosity, the thinner the ligaments and the smaller the nodes (i.e., intersection or joint of ligaments). Fig. 8(c) depicts corresponding changes in fluid volume and shape as porosity is increased.

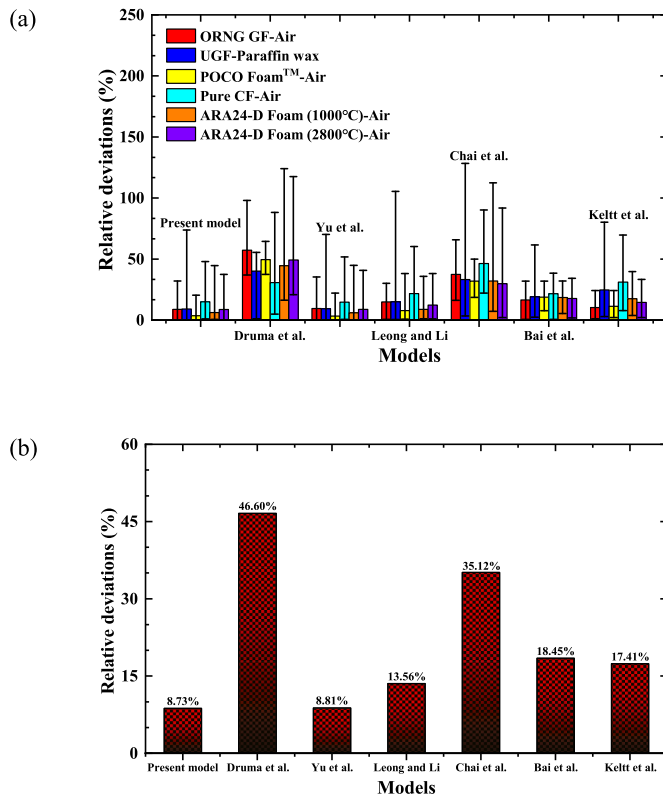


Fig. 13. Relative deviations (RDs) comparison: (a) different effective conductivity models for selected graphite foams; (b) average RDs for various effective conductivity models.

4. Results and discussion

4.1. Permeability

4.1.1. Model validation

In sharp contrast to effective thermal conductivity, previous studies are rarely concerned with theoretically determining the permeability of graphite foams. Therefore, existing experimental results [54,55] and the current simulation data are employed to verify the present permeability model. Table 5 compares the predicted permeability values with those experimentally measured; relevant pore parameters including ε , λ and d_p are also listed. To quantitatively analyze the accuracy of model predictions, relative deviation (RD) is defined, as:

$$RD = \left| \frac{K_{pre} - K_{exp}}{K_{exp}} \right| \quad (48)$$

where the subscripts “exp” and “pre” represent prediction and experiments, in respective.

The foam sample tested by Leong et al. [54] has a porosity of 0.75 and a pore size of 310 μm . Based on the scanning electron microscopy (SEM) image provided by these authors, the ligament thickness of the foam is estimated as 110 μm . As to the sample tested by Straatman et al. [55], the porosity is 0.82, the pore size is 500 μm , and the ligament thickness is calculated using the empirical correlation [56], $\frac{d_l}{d_p} = 1.18 \sqrt{\frac{1-\varepsilon}{3\pi}} \left(\frac{1}{1-e^{-(1-\varepsilon)/0.04}} \right)$, as 82.3 μm . It can be seen from Table 5 that a maximal deviation less than 0.7% is achieved between model prediction and experimental measurement, thus demonstrating the validation of the proposed fractal permeability model.

To enrich the diversity of porosity for graphite foam, 13 geometry models with porosities ranging from 0.686 to 0.918 are constructed for direct numerical simulation; Table 4 presents detailed parameters of

these geometry models. Fig. 9 compares the permeabilities obtained by model predictions and numerical simulations and, again, satisfactory agreement is achieved, further illustrating the verification of the model.

4.1.2. Pore-scale features for fluid flow

Fig. 10 demonstrates how the numerically simulated pore-scale velocity field in a graphite foam varies with its porosity. Increasing the porosity reduces ligament thickness and hence the resistance of ligaments to fluid flow. Macroscopically, fluid pressure drop through the graphite foam cell decreases, increasing permeability. Since the inlet and outlet of the graphite foam cell are set as periodic translational boundaries for constant mass flow, the velocity field in the central region of the cell decreases with increasing porosity in Fig. 10(a). A higher porosity with a fixed mass flow rate leads to a larger pore window area, causing the pore-scale velocity to decrease.

Fig. 11 presents the distribution of streamlines in selected graphite foam cells. In Fig. 11(a), the pores around the cell edges are blocked by ligaments. Streamlines in the A area of Fig. 11(a) cannot enter the pores of adjacent edges, but can enter the pore located in the center of the cell via a small pore connected to the central pore. As the porosity is increased, the ligaments thickness decreases such that the edge pores are increasingly connected, as shown in Fig. 11(b). Thus, the streamlines can enter the central pore and the peripheral pores from the A area, respectively. It can be found from areas B and C in Fig. 11 that the presence of solid ligaments increases the streamline tortuosity. This indicates that the distribution of ligaments in a graphite foam is one of the main factors affecting its permeability. For the area D in Fig. 11, the streamline passes directly through the small circular pore located at the center of entrance surface and enters the central pore area: the streamline tortuosity is therefore much smaller in the D area. In Fig. 11(a), the fluid cannot enter the E area, due mainly to the blockage of ligaments. On the contrary, the edge pores are connected in Fig. 11(b) and hence the fluid can enter the E area. In addition, the proportion of high-speed streamlines (marked in red) in Fig. 11(a) is higher than that in Fig. 11(b) due to two main reasons. On the one hand, as the porosity increases from Fig. 11(a)–(b), the proportion of ligaments decreases in Fig. 11(b); under the condition of constant mass periodic flow, the speed of streamlines is relatively fast in Fig. 11(a). On the other hand, as the blocking effect of ligaments makes it almost impossible for the fluid to enter the E area in Fig. 11(b), the pore volume passed by the fluid decreases, thus increasing the fluid velocity. Under the combined actions of the two factors, the fluid velocity in Fig. 11(a) is larger than that in Fig. 11(b).

4.2. Effective thermal conductivity

4.2.1. Model validation

To validate the proposed fractal model of effective thermal conductivity for graphite foams, existing measurement data [20,24,52,53,55] (Table 6) and theoretical predictions with alternative models [24,34–37, 57,58] are both employed. Details of existing theoretical models are summarized in Table 1; corresponding effective conductivity calculations by these models are based on the properties listed in Table 3. As shown in Fig. 12, satisfactory agreement between the fractal model prediction and measurement data is achieved. Further, the proposed fractal model demonstrates a better agreement than most alternative models [24,34–37,57,58] presented in Table 1. The models of the Druma et al.’s and the Chai et al.’s always led to overestimated effective conductivities for a wide range of graphite foams considered. In contrast, within the porosity range of $0.65 \leq \varepsilon \leq 0.72$, the predictions of the Leong et al.’s model are smaller than experimental (or simulation) data. The models developed by Yu et al. [35] and Klett et al. [24] satisfactorily predicted the variation trends of conductivity with porosity; nonetheless, the model of Klett et al. contains empirical (or fitting) parameters. When the porosity is greater than 0.85, the predicted value of the Bai et al.’s model is in good agreement with the

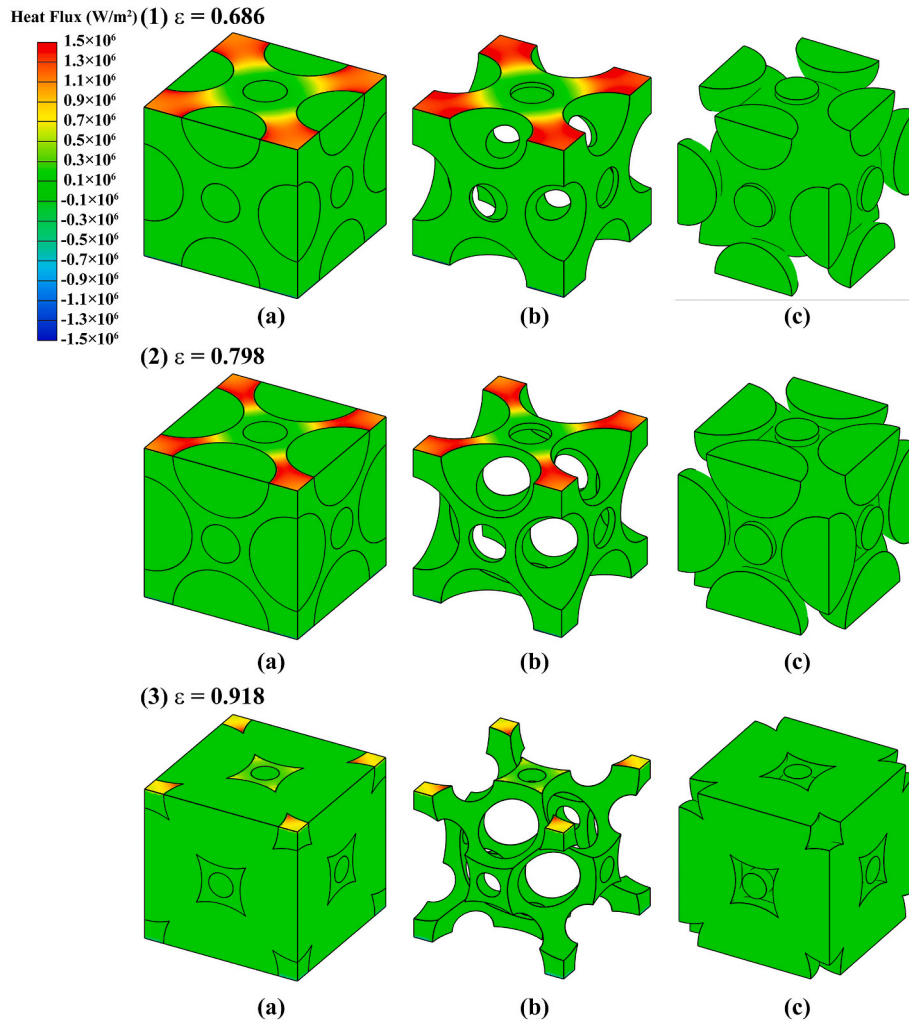


Fig. 14. Heat flux distribution: (a) graphite foam assembly; (b) top view of graphite foam solid phase; (c) top view of graphite foam fluid phase.

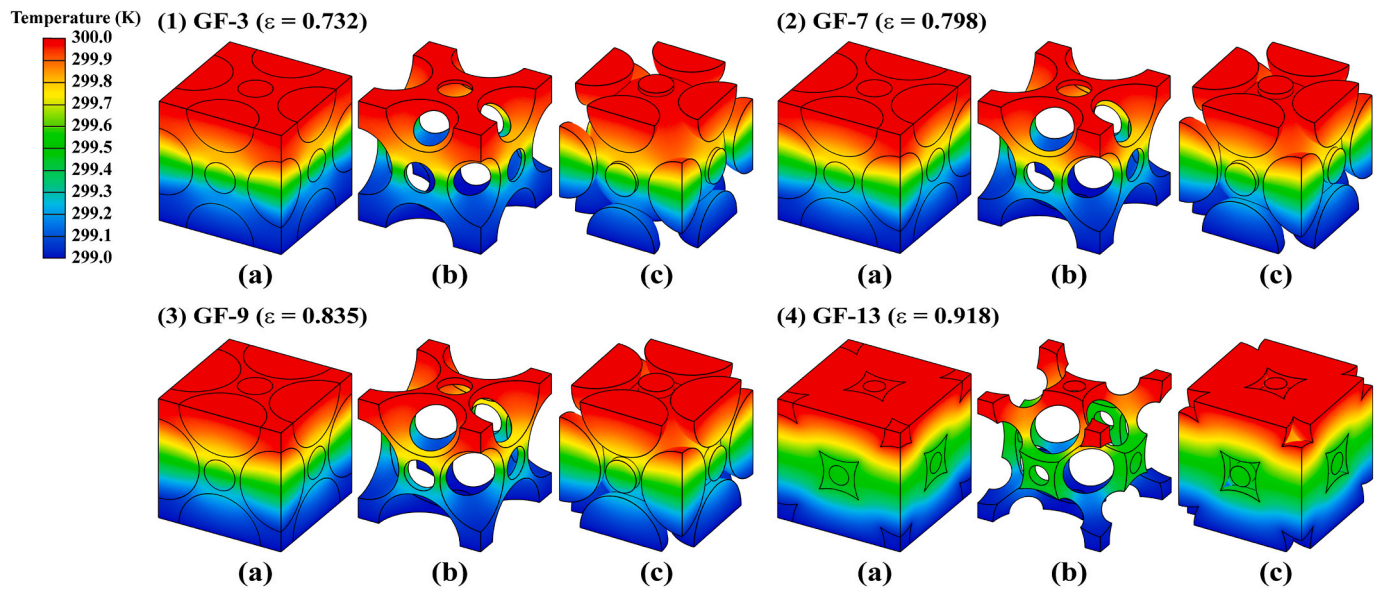


Fig. 15. Influence of porosity on temperature distribution in (a) graphite foam assembly, (b) solid phase, and (c) fluid phase.

experimental and simulated data. However, the model underestimates the effective thermal conductivity of all graphite foams when the porosity is less than 0.85. In addition to the above comparison between model predictions and measurements, effective conductivity results obtained from pore-scale numerical simulations are also employed for comparison: satisfactory agreement with experimental data and theoretical predictions is achieved, as shown in Fig. 12.

In Fig. 13(a), relative deviation (RD) is used to evaluate the accuracy of different effective conductivity models, and the current fractal model is seen to give better predictions than other models. For air-saturated ORNG GF and ARA24-D Foam, the RDs of the current model are lower than the Yu et al. model which provides good predictions among the existing models considered. For paraffin wax-saturated UGF, the RD of the current model is also lower than that of other models. Fig. 13(b) presents the average RD values obtained by mathematical manipulations on the arithmetic mean of all data available. As seen in Fig. 13(b), the current model, with an average deviation of 8.73%, has the lowest RD amongst all the models considered, followed by the Druma et al. model (46.60%), the Yu et al. model (8.81%), the Leong-Li model (13.56%), the Chai et al. model (35.12%), the Bai et al. model (18.45%), and the Klett et al. model (17.41%). Although the Klett et al. model demonstrates a comparably low RD value, the model is naturally semi-analytical because it contains fitted parameters with no physical meanings. According to fractal theory for porous media, present model better predicts the effective conductivity compared to existing models, thus proving the feasibility of using fractal theory to explore heat conduction in graphite foams. The fractal theory entirely takes in consideration of the randomness of pore size and distribution, in consistence with the actual pore morphology in graphite foams.

The current graphite foam model describes the pore micro-topology and surface topography in detail, focusing on the important fractal characteristics of randomly distributed pores. Therefore, the analytical model (Eq. (46)) can more accurately predict the effective thermal conductivity of graphite foam, thus providing a reference for the design and improvement of graphite foam in thermal storage and thermal management applications. In the current study, the relationship between the effective thermal conductivity and porosity of various graphite foams is predicted with good agreement. Graphite foam here is mainly filled with air and paraffin wax. On the one hand, the effective thermal conductivity of air-saturated graphite foam can provide theoretical guidance for the design and utilization of compact heat exchangers. On the other hand, paraffin wax-saturated graphite foam can be used to prepare high-performance latent heat thermal storage system.

4.2.2. Pore-scale features of heat conduction

Fig. 14 demonstrates the heat flux distribution on pore structures having different porosities. It can be seen from Fig. 14(b) that the heat flux variation is mainly concentrated in the solid phase, with almost no change in heat flux for the fluid phase. The main physical reason is that the fluid phase is air whose thermal conductivity (0.023 W/(m·K)) is much smaller than that of graphite ligament (1300 W/(m·K)). This indicates that the thermal conductivity of a graphite foam is mainly concentrated in solid ligaments, and the interstitial fluids play a negligible role in heat conduction. As shown in Fig. 14, the heat flux on the ligament surface decreases with increasing porosity, mainly caused by the corresponding reduction in solid phase ratio. Therefore, the effective conductivity significantly decreases when the porosity gradually increases. While the variation of heat flux is mainly distributed around the solid phase, such variation in the central region of the solid phase is smaller in Fig. 14(a) and (b). This indicates that heat conduction mainly occurs along the *s*-axis from top to bottom, with more negligible conduction within the face.

Fig. 15 illustrates temperature distribution in graphite foam assembly, solid phase, and fluid phase for geometry models with selected porosities. It can be found from Fig. 15(a) that temperature distributions in solid and fluid phases are different and are distinctively altered as foam porosity is varied. With increasing porosity, the area for the high-temperature range at the top region gradually reduces and that for the low-temperature range at the bottom region decreases, which together cause the area of the medium-temperature region to increase. A higher porosity results in thinner ligaments, thereby reducing their heat conduction capability (i.e., heat flux decreases). Heat is therefore accumulated at the top region. As for the low-temperature range, similar phenomenon exists when the porosity is increased, thus further illustrating the decrease of effective conductivity with increasing porosity. Although the overall heat conduction follows the *z*-axis from top to bottom, the isotherm is not perpendicular to the direction of heat conduction (*z*-axis), because the pore structure alters local temperature gradient, i.e., heat conduction lines become tortuous. This illustrates that the pore structure of a graphite foam is an important factor affecting its effective conductivity. The effective conductivity may vary significantly for the same porous material as its pore structure is altered.

5. Conclusion

Previous prediction models of conductivity and permeability seldomly considered the effects of random distributions of pore shape and size intrinsically induced during processing of the graphite foam. To rectify this problem, analytical models of permeability as well as conductivity for graphite foam are developed based on fractal theory. In parallel, pore-scale numerical simulations are carried out, providing not only cross-validation but also shedding light on transport mechanisms at pore level. Analytical model predictions and numerical simulation results are both compared with existing experimental data. Fractal model satisfactorily predict the two transport properties, with validated by measurement data. The following conclusion can be drawn.

- (1) The permeability of graphite foam can be analytically expressed as a function of porosity ϵ , pore size λ , characteristic length L_0 , cross-sectional area A , and fractal dimensions (D_T and D_f), and relevant parameters all have physical meaning and explanations.
- (2) In the range of foam porosity from 0.686 to 0.918, the permeability model predictions are in good agreement with pore-scale numerical simulation results.
- (3) The effective thermal conductivity of graphite foam can be functioned analytically with porosity ϵ , fractal dimensions (D_T and D_f), and constituent conductivities (k_f and k_s).
- (4) Compared to existing models of effective thermal conductivity, the current fractal model achieves the smallest deviation (average of 8.73%) for graphite foams having different parent ligament materials and filling fluids (air and paraffin wax).

The current study more comprehensively considers the influence factors of graphite foam on permeability and effective thermal conductivity. Meanwhile, the current models can more accurately predict the permeability and the effective thermal conductivity of graphite foam. In addition, porous media are often regarded as continuous media in numerical simulation. Thus, the selection of physical parameters in the equation is related to the accuracy of numerical simulation results, such as permeability and effective thermal conductivity. Therefore, the current analytical model can provide theoretical guidance for engineering applications.

Declaration of competing interest

The authors declare that they have no known competing financial interests or personal relationships that could have appeared to influence the work reported in this paper.

Data availability

Data will be made available on request.

Acknowledgements

This work was supported by the National Natural Science Foundation of China (51976155 and 12032010). Xiaohu Yang gratefully acknowledged the support of K. C. Wong Education Foundation.

References

- J. Zhao, A. Ozden, S. Shahgaldi, I.E. Alaefour, X. Li, F. Hamdullahpur, Effect of Pt loading and catalyst type on the pore structure of porous electrodes in polymer electrolyte membrane (PEM) fuel cells, *Energy* 150 (2018) 69–76.
- A. Mallow, O. Abdelaziz, S. Graham, Thermal charging performance of enhanced phase change material composites for thermal battery design, *Int. J. Therm. Sci.* 127 (2018) 19–28.
- G. Zhang, L. Wu, Z. Qin, J. Wu, F. Xi, G. Mou, Y. Wang, K. Jiao, A comprehensive three-dimensional model coupling channel multi-phase flow and electrochemical reactions in proton exchange membrane fuel cell, *Adv. Appl. Energy* 2 (2021) 100033.
- H.W. Son, C.S. Heu, H.S. Lee, S.H. Kim, J.Y. Mok, S.-W. Kang, D.R. Kim, Enhanced thermal performance of lithium nitrate phase change material by porous copper oxide nanowires integrated on folded meshes for high temperature heat storage, *Chem. Eng. J.* 391 (2020) 123613.
- N. Zhang, Y. Yuan, Synthesis and thermal properties of nanoencapsulation of paraffin as phase change material for latent heat thermal energy storage, *Energy Built Environ.* 1 (2020) 410–416.
- J.J. Ijeje, Q. Gan, J. Cai, Influence of permeability anisotropy on heat transfer and permeability evolution in geothermal reservoir, *Adv. Geo-Energy Res.* 3 (2019) 43–51.
- S. Shuja, B. Yilbas, M. Kassas, Flow over porous blocks in a square cavity: influence of heat flux and porosity on heat transfer rates, *Int. J. Therm. Sci.* 48 (2009) 1564–1573.
- A. Vecchi, Y. Li, Y. Ding, P. Mancarella, A. Sciacovelli, Liquid air energy storage (LAES): a review on technology state-of-the-art, integration pathways and future perspectives, *Adv. Appl. Energy* 3 (2021) 100047.
- E.M. Thaysen, S. McMahon, G.J. Strobel, I.B. Butler, B.T. Ngwenya, N. Heinemann, M. Wilkinson, A. Hassanpouryouzband, C.I. McDermott, K. Edlmann, Estimating microbial growth and hydrogen consumption in hydrogen storage in porous media, *Renew. Sustain. Energy Rev.* 151 (2021) 111481.
- F. Hosseini, M. Siavashi, Optimization of SMR process for syngas production through a solar-assisted thermo-chemical reactor with a multi-layered porous core, *Sol. Energy* 230 (2021) 208–221.
- A. Akbar, J. Liu, S.-J. Chung, S. Um, Statistical characterization of non-linear microscopic mechanical deformation through randomly oriented fibrous porous transport layers for advanced electrochemical energy systems, *Renew. Energy* 178 (2021) 1106–1118.
- H. Pourrahmani, M. Moghimi, M. Siavashi, Thermal management in PEMFCs: the respective effects of porous media in the gas flow channel, *Int. J. Hydrogen Energy* 44 (2019) 3121–3137.
- X. Xiao, P. Zhang, M. Li, Effective thermal conductivity of open-cell metal foams impregnated with pure paraffin for latent heat storage, *Int. J. Therm. Sci.* 81 (2014) 94–105.
- H. Li, Z. Wang, T. Hong, M.A. Piette, Energy flexibility of residential buildings: a systematic review of characterization and quantification methods and applications, *Adv. Appl. Energy* 3 (2021) 100054.
- X. Yang, T. Lu, T. Kim, Thermal stretching in two-phase porous media: physical basis for Maxwell model, *Theor. Appl. Mech. Lett.* 3 (2013), 021011.
- X.H. Yang, T.J. Lu, T. Kim, A simplistic model for the tortuosity in two-phase close-celled porous media, *J. Phys. Appl. Phys.* 46 (2013) 125305.
- W. Lin, J. Yuan, B. Sundén, Review on graphite foam as thermal material for heat exchangers, in: *World Renewable Energy Congress 2011, WREC*, 2011, p. 2011.
- J. Guo, Z. Du, G. Liu, X. Yang, M.-J. Li, Compression Effect of Metal Foam on Melting Phase Change in a Shell-And-Tube Unit, *Applied Thermal Engineering*, 2022, p. 118124.
- J. Guo, Z. Liu, Z. Du, J. Yu, X. Yang, J. Yan, Effect of fin-metal foam structure on thermal energy storage: an experimental study, *Renew. Energy* 172 (2021) 57–70.
- J. Klett, R. Hardy, E. Romine, C. Walls, T. Burchell, High-thermal-conductivity, mesophase-pitch-derived carbon foams: effect of precursor on structure and properties, *Carbon* 38 (2000) 953–973.
- A.G. Straatman, N.C. Gallego, Q. Yu, L. Betchen, B. Thompson, Forced convection heat transfer and hydraulic losses in graphitic foam, *J. Heat Trans. ASME* 129 (2007) 1237–1245.
- N.C. Gallego, J.W. Klett, Carbon foams for thermal management, *Carbon* 41 (2003) 1461–1466.
- J. Paek, B. Kang, S. Kim, J.M. Hyun, Effective thermal conductivity and permeability of aluminum foam materials 1, *Int. J. Thermophys.* 21 (2000) 453–464.
- J.W. Klett, A. McMillan, N. Gallego, C. Walls, The role of structure on the thermal properties of graphitic foams, *J. Mater. Sci.* 39 (2004) 3659–3676.
- J. Klett, B. Conway, Thermal management solutions utilizing high thermal conductivity graphite foams, in: *Society for the Advancement of Material and Process Engineering, Bridging the Centuries with SAMPE's Materials and Processes Technology* 45, 2000, pp. 1933–1943.
- G. Gürüf, İ. Solmuş, K. Bilen, Ö. Bayer, Experimental based numerical approach for determination of volumetric heat transfer coefficients of modified graphite foams, *Appl. Therm. Eng.* 174 (2020) 115310.
- F. Moglie, D. Micheli, S. Laurenzi, M. Marchetti, V.M. Primiani, Electromagnetic shielding performance of carbon foams, *Carbon* 50 (2012) 1972–1980.
- J. Li, G. Zhang, X. Fan, Q. Gao, H. Zhang, J. Qin, X. Shi, X. Fang, Microcellular epoxy/reduced graphene oxide/multi-walled carbon nanotube nanocomposite foams for electromagnetic interference shielding, *Appl. Surf. Sci.* 552 (2021) 149232.
- A. Fethi, L. Mohamed, K. Mustapha, B.N. Sassi, Investigation of a graphite/paraffin phase change composite, *Int. J. Therm. Sci.* 88 (2015) 128–135.
- B. Shang, R. Wu, J. Hu, R. Hu, X. Luo, Non-monotonously tuning thermal conductivity of graphite-nanosheets/paraffin composite by ultrasonic exfoliation, *Int. J. Therm. Sci.* 131 (2018) 20–26.
- K. Chintakrinda, R.D. Weinstein, A.S. Fleischer, A direct comparison of three different material enhancement methods on the transient thermal response of paraffin phase change material exposed to high heat fluxes, *Int. J. Therm. Sci.* 50 (2011) 1639–1647.
- K. Hooman, N. Dukhan, A theoretical model with experimental verification to predict hydrodynamics of foams, *Transport Porous Media* 100 (2013) 393–406.
- Z. Hashin, S. Shtrikman, A variational approach to the theory of the effective magnetic permeability of multiphase materials, *J. Appl. Phys.* 33 (1962) 3125–3131.
- A.M. Druma, M.K. Alam, C. Druma, Analysis of thermal conduction in carbon foams, *Int. J. Therm. Sci.* 43 (2004) 689–695.
- Q. Yu, B.E. Thompson, A.G. Straatman, A unit cube-based model for heat transfer and fluid flow in porous carbon foam, *J. Heat Trans. ASME* 128 (2006) 352–360.
- K. Leong, H. Li, Theoretical study of the effective thermal conductivity of graphite foam based on a unit cell model, *Int. J. Heat Mass Tran.* 54 (2011) 5491–5496.
- Y. Chai, X. Yang, M. Zhao, Z. Chen, X. Meng, L. Jin, Q. Zhang, W. Hu, Study of microstructure-based effective thermal conductivity of graphite foam, *J. Heat Tran.* 139 (2017), 052004.
- B. Xiao, Q. Huang, H. Chen, X. Chen, G. Long, A fractal model for capillary flow through a single tortuous capillary with roughened surfaces in fibrous porous media, *Fractals* 29 (2021) 2150017.
- X. Qin, Y. Zhou, A.P. Sasmito, An effective thermal conductivity model for fractal porous media with rough surfaces, *Adv. Geo-Energy Res.* 3 (2019) 149–155.
- J. Cai, Z. Zhang, W. Wei, D. Guo, S. Li, P. Zhao, The critical factors for permeability-formation factor relation in reservoir rocks: pore-throat ratio, tortuosity and connectivity, *Energy* 188 (2019) 116051.
- B.B. Mandelbrot, B.B. Mandelbrot, *The Fractal Geometry of Nature*, WH freeman, New York, 1982.
- B. Yu, P. Cheng, A fractal permeability model for bi-dispersed porous media, *Int. J. Heat Mass Tran.* 45 (2002) 2983–2993.
- B. Yu, J. Li, Some fractal characters of porous media, *Fractals* 9 (2001) 365–372.
- B. Xiao, W. Wang, X. Zhang, G. Long, J. Fan, H. Chen, L. Deng, A novel fractal solution for permeability and Kozeny-Carman constant of fibrous porous media made up of solid particles and porous fibers, *Powder Technol.* 349 (2019) 92–98.
- M. Liang, C. Fu, B. Xiao, L. Luo, Z. Wang, A fractal study for the effective electrolyte diffusion through charged porous media, *Int. J. Heat Mass Tran.* 137 (2019) 365–371.
- B. Xiao, Y. Zhang, Y. Wang, G. Jiang, M. Liang, X. Chen, G. Long, A fractal model for Kozeny-Carman constant and dimensionless permeability of fibrous porous media with roughened surfaces, *Fractals* 27 (2019) 1950116.
- B.-M. Yu, Fractal character for tortuous streamtubes in porous media, *Chin. Phys. Lett.* 22 (2005) 158.
- T. Xiao, X. Yang, K. Hooman, T.J. Lu, Analytical fractal models for permeability and conductivity of open-cell metallic foams, *Int. J. Heat Mass Tran.* 177 (2021) 121509.
- F.A. Dullien, *Porous Media: Fluid Transport and Pore Structure*, Academic press, 2012.

- [50] M. Yun, B. Yu, P. Xu, J. Wu, Geometrical models for tortuosity of streamlines in three-dimensional porous media, *Can. J. Chem. Eng.* 84 (2006) 301–309.
- [51] B. Yu, P. Cheng, Fractal models for the effective thermal conductivity of bidispersed porous media, *J. Thermophys. Heat Tran.* 16 (2002) 22–29.
- [52] P. Jana, V. Fierro, A. Pizzi, A. Celzard, Thermal conductivity improvement of composite carbon foams based on tannin-based disordered carbon matrix and graphite fillers, *Mater. Des.* 83 (2015) 635–643.
- [53] E. Fleming, I. Kholmanov, L. Shi, Enhanced specific surface area and thermal conductivity in ultrathin graphite foams grown by chemical vapor deposition on sintered nickel powder templates, *Carbon* 136 (2018) 380–386.
- [54] K. Leong, H. Li, L. Jin, J. Chai, Convective heat transfer in graphite foam heat sinks with baffle and stagger structures, *J. Heat Tran.* 133 (2011), 060902.
- [55] A. Straatman, N. Gallego, Q. Yu, B. Thompson, Characterization of porous carbon foam as a material for compact recuperators, *J. Eng. Gas Turb. Power-Trans. ASME* 129 (2007) 326–330.
- [56] A. Bhattacharya, V.V. Calmidi, R.L. Mahajan, Thermophysical properties of high porosity metal foams, *Int. J. Heat Mass Tran.* 45 (2002) 1017–1031.
- [57] X. Bai, A. Nakayama, Quick estimate of effective thermal conductivity for fluid-saturated metal frame and prismatic cellular structures, *Appl. Therm. Eng.* 160 (2019) 114011.
- [58] X. Bai, Z. Zheng, C. Liu, A. Nakayama, Metal frame structures with controlled anisotropic thermal conductivity, *Int. J. Heat Mass Tran.* 148 (2020) 119064.